ACS Editors' Choice

ACS Chemical Neuroscience

Research Article

pubs.acs.org/chemneuro

Hyperspectral Imaging Signatures Detect Amyloidopathy in Alzheimer's Mouse Retina Well before Onset of Cognitive Decline

Swati S. More and Robert Vince*

Center for Drug Design, University of Minnesota, 516 Delaware Street S.E., Minneapolis, Minnesota 55455, United States

Ⓢ *Supporting Information*

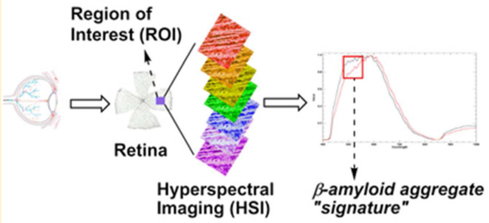

ABSTRACT: Amyloidopathic disorders such as Alzheimer's disease present symptomology years after the entrenchment of amyloidogenic imbalance. The pathologic α-helix → β-strand conversion of amyloid β^{1-42} and amyloid β^{1-40} peptides causes neuronal death in the vicinity. Symptomology often presents only after significant neurodegeneration. This thus warrants early detection of amyloidopathy in Alzheimer's disease. Nonexistent modalities for direct identification and quantitation of soluble amyloid aggregates or (proto)fibrils forced us to undertake the development of a spectrophotometric technique to support ongoing drug design. Key requirements were independence from the need for extraneous staining, unambiguous amyloid aggregate detection, and minimal influence of interpretative errors. A Cytoviva instrument pivotal to this study captures scattering of light of visible−near-infrared (VNIR, 400−1000 nm) wavelengths within each pixel of the microscopic view field. We thus assembled a scattering intensity pattern database that provided "signatures" of amyloid aggregates. Comparison of unknown samples against this database enabled direct detection of amyloid aggregates. The technique was found useful for monitoring retinal and brain amyloidopathy in an ongoing preclinical anti-AD study, attesting to the technique's sensitivity and specificity. Interestingly, the technique was found applicable not just to excised brain tissue but also to isolated mouse retina. With the retina being heralded widely as a (diagnostic) extension of the CNS and retinal amyloidopathy occurring well before that in the brain, this development raises a possibility for the first direct retinal imaging diagnosis of early asymptomatic Alzheimer's disease.

KEYWORDS: *Hyperspectral imaging (HSI), Alzheimer's disease, β-amyloid peptide, methylglyoxal, advanced glycation end products*

Protein folding constitutes ordering of an existing polypeptide or one progressively emerging from translation in a histone, into secondary or higher order structures. Protein conformation is a primary determinant of physiological or pathological function.[1] Although regulated strictly by translational sequence, noncovalent interactions with molecular chaperones, and degradative proteolysis, protein folding is hardly infallible. A majority of misfolded proteins and peptides are either granted another chance to fold correctly (through de- or reglycosylation), halted from further folding by heat-shock proteins, or labeled for destruction (e.g., ubiquitination). Extracellularly, phagocytosis and general proteolysis act as controls;[2] some persist nevertheless. Some are toxic on their own accord; others elicit toxicity by homo- or hetero-oligomerization. The latter mechanism resembles prion propagation[3] and is a major symptomological or etiological component of protein misfolding diseases.[4] Examples are Alzheimer's disease, type-II diabetes, and Huntington's disease.[5] Frequently, the polypeptide that misfolds is produced in large quantities.[6] Alzheimer 's disease (AD) molecular pathology showcases a consequence of the misfolding of the amyloid peptide fragments ($A\beta^{1-40}$, $A\beta^{1-42}$) that are produced during proteolysis of the membrane associated amyloid precursor protein.[7,8] The amyloid peptides (particularly $A\beta^{1-42}$) are inherently disordered in their native forms. A lipid environment promotes a metastable α-helical conformation, while extracellular space promotes extended conformations. An $A\beta$ peptide in extended conformations can aggregate into soluble oligomers and then into metastable globular colloids (clustering around a diameter of ~20 nm) or "critical oligomers".[9] Further aggregation of this colloid, possibly through dipoles borne by α-sheets, leads to rod-like "protofibrils" whose length lies in the 50−500 nm range.[10] Further aggregation results in insoluble fibrils of crystalline habit[11] that may coalesce into plaques.[12] The aforementioned is not the only possible fate of an errant $A\beta$ peptide; a variety of metastable states and fibril morphologies are known to exist. Worrisome examples are the "globulomers", hollow-core colloids (2−6 nm), and hollow-core soluble protofibrils (20−200 nm) that can reside in the lipid bilayer cell membrane, effectively creating a nonselective channel that can compromise cellular homeostasis.[13,14] Soluble amyloid aggregates (s$A\beta$) of the aforementioned orders are becoming increasingly apparent as the pathogenic entities that induce cognitive decline and neurodegeneration, with specific molecular pathology of well-defined species being known in some cases (e.g., *N*-methyl-D-aspartate receptor (NMDAR) mediated neurotoxicity caused by s$A\beta$).[15]

Received: October 8, 2014
Accepted: October 29, 2014
Published: October 29, 2014

dx.doi.org/10.1021/cn500242z | *ACS Chem. Neurosci.* 2015, 6, 306−315

Early cognitive decline associated with AD (eAD) may very well be the first clinically tractable pathology, but by then, metastasis of the misfolded protein has already established its fatal course.[16] The phase-III clinical trial of bapinuzumab (an antibody that targets Aβ plaque) has clearly underscored the need for early detection and address of amyloidopathy.[17] In theory, interrupting the early stage of amyloidopathy with small molecules presents a solution; however, the utter lack of suitable diagnostic tools for both *in vivo* rapid screening of small molecule Aβ aggregation inhibitors and early detection of AD pathology pose severe hindrances. Extant molecular screens (even advanced models such as the Neurovision Eye Test[18]) for misfolded Aβ are cell-free and employ dyes (e.g., thioflavin-T, congo red) whose binding to Aβ fibrils causes characteristic spectral shift.[19] Unfortunately, this needs an extraneous agent and is additionally subject to variance in the presence of small molecules, as would be the case during an inhibitor screen reliant upon fluorescent probes. Mass-spectrometry based screens such as that of Zovo et al. are able to identify Aβ fibrillogenesis inhibitors but not those of Aβ oligomerization.[20] Cell-culture and cytotoxicity models still remain the mainstay of Aβ aggregation inhibitor screening. All of the existing models of this type employ altered forms of Aβ (such as a GFP−Aβ hybrid and FITC-labeled Aβ peptides) that would aid detection[21] or require concentrations of the Aβ peptide at which the latter becomes impractically expensive if it were to be used for a drug discovery or development screen.[22]

This paper serves to disclose an implementation of imaging spectroscopy whose resolution of two-dimensional space and of the visible−near-IR portion of the electromagnetic spectrum achieves extents that enable identification of assemblies consisting of $A\beta^{1-42}$, particularly of sAβ aggregates. The core principle may be stated as follows: a pixel is one unit area of known location and dimensions within a microscopic field of view. When illuminated, the interference of each pixel (qualitative and quantitative) with traversing light radiation is dictated by the optical characteristics of its components and the composition (spectrum) of the incident light. These characteristics can be light transmittance, absorption, and scatter. All of these are reflected in the spectrum (intensity vs wavelength plot) of light emanating from an area. The relative variances in intensities across differing wavelengths are characteristics unique to the optical features within the area. The ability of an imaging spectroscopy to identify such unique characteristics of a unit area will depend directly on (1) the number of wavelengths within the spectrum whose intensities can be measured independently of other wavelengths (spectral resolution) and (2) the precision and accuracy in intensity quantification of a unit wavelength. The spectrum obtained is a multiorder result of optical phenomena contributed by features within the area being imaged. The size of a unit area within the field being imaged (pixel size) will thus be inversely proportional to the number of distinct, indivisible optical features that can be practically identified in the spectrum of the area. Spatial "resolution" here is effectively the number of pixels within a known area (e.g, "1 in.^{2}") that can be imaged distinctly and independently of each other and has two dimensions (x and y, the Cartesian coordinates). Over n wavelengths, a pixel yields n number of light intensities (the third or "spectral" dimension). Conventionally, when intensities of 100−999 distinct wavelengths are recorded, the prefix "hyperspectral" is applied to the imaging spectroscopy technique. When this spectral resolution is coupled with a magnification system (such as a microscope) that produces sub-micrometer resolution, the resultant spectra (relative intensity variance patterns) are of sufficiently low order such that direct representation of indivisible optical features is attained.

The remnant variable is the signal-to-noise (S/N) ratio, which in the presence of directly transmitted light would be far too low, the objects sought being colloidal in nature (and likely lower in abundance than the transparent elements in the specimen) and thus not altering significantly the spectrum emanating from the specimen. Transmitted light is thence blocked (i.e., dark-field conditions) and a rather effective (and proprietary) illumination system (Cytoviva, described under Methods) is employed to compensate for lost illumination. The emergent spectrum now is purely one from light absorption and scatter, which combined with the spatiospectral resolution described above yields satisfactorily high S/N ratios.

Specific goals pursued in this study are (1) to determine whether hyperspectral imaging of cytoplasm highlights any characteristic trends that correlate with Aβ aggregation, (2) to explore the feasibility of building a library of "Aβ aggregation signatures", thus laying the foundation for a diagnostic tool, (3) to examine the effects of Aβ aggregation inhibitors on hyperspectral images, so as to examine sensitivity of the method and its compatibility with treatment regimens of common age-related disorders, and finally (4) to provide *ex vivo* method validation by tracking progress of an investigational treatment and the disease itself in the transgenic Alzheimer's mouse model.

■ RESULTS AND DISCUSSION

HSI Spectral Signature of $A\beta^{1-42}$ Aggregates. Net uptake of N-terminal fluorescein isothiocyanate labeled $A\beta^{1-42}$ (FITC−$A\beta^{1-42}$) into SH-SY5Y cells at 0−1000 nM exposure levels led to proportional rise in intracellular fluorescence, confirming intracellular accumulation of $A\beta^{1-42}$ (data not shown).[23] Organelle distribution data is inconsequential to the purpose of this experiment, but excellent reports are available from others discussing trafficking of Aβ into late lysosomes and derivative vesicles.[24] Figure 1 shows a HSI spectrum of SH-SY5Y cells that were treated with scrambled $A\beta^{1-42}$ (scr-$A\beta^{1-42}$, nonaggregation prone control), juxtaposed with cells treated

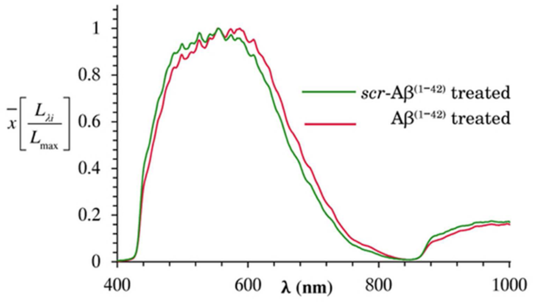

Figure 1. Cytoplasmic changes caused by the uptake of $A\beta^{1-42}$ peptide (250 nM) in SH-SY5Y cells were detected by hyperspectral imaging after an incubation period of 24 h. Spectral information in the range of 400−1000 nm was extracted from cytoplasmic regions of interest (ROIs) as described under Methods. The figure shows a "mean spectrum" (i.e., arithmetic means of intensities at all measured wavelengths vs wavelengths) of 15 ROIs from the cytoplasm of $A\beta^{1-42}$ treated (red) and nontreated (scrambled $A\beta^{1-42}$ peptide treated, green) cells.

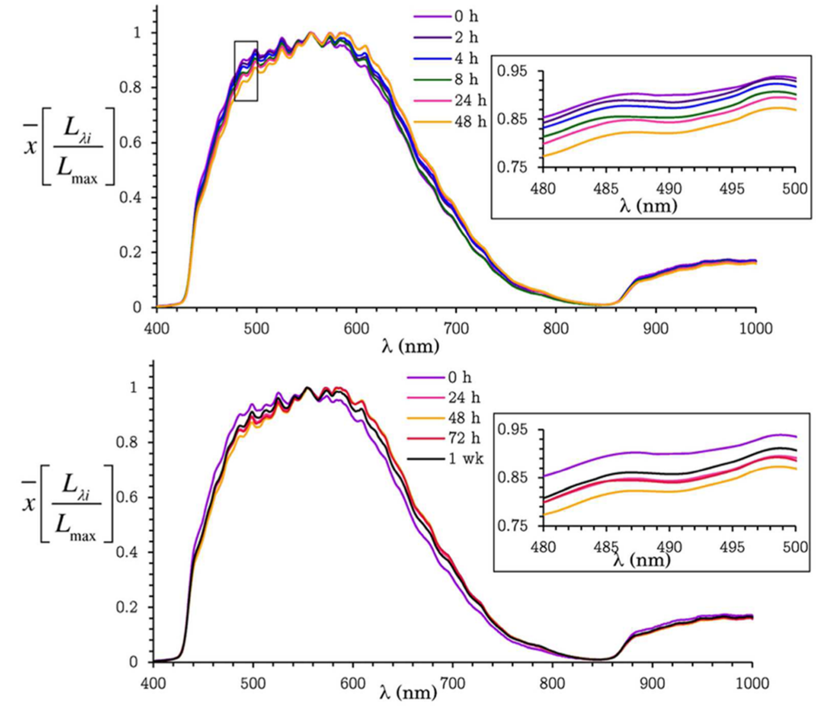

Figure 2. (A) Time-dependence of cytoplasmic changes caused by Aβ^{1-42}. SH-SY5Y cells were exposed to Aβ^{1-42} peptide (250 nM) for varying time intervals, and hyperspectral data was collected from the cytoplasm of cells. Spectral changes were apparent as early as 4 h of incubation with Aβ^{1-42} with maximal spectral change being observed at the 48 h mark. (B) Spectral differences between cells treated and not-treated with Aβ^{1-42} began reducing beyond 48 h, with this trend persisting until the end of 1 week.

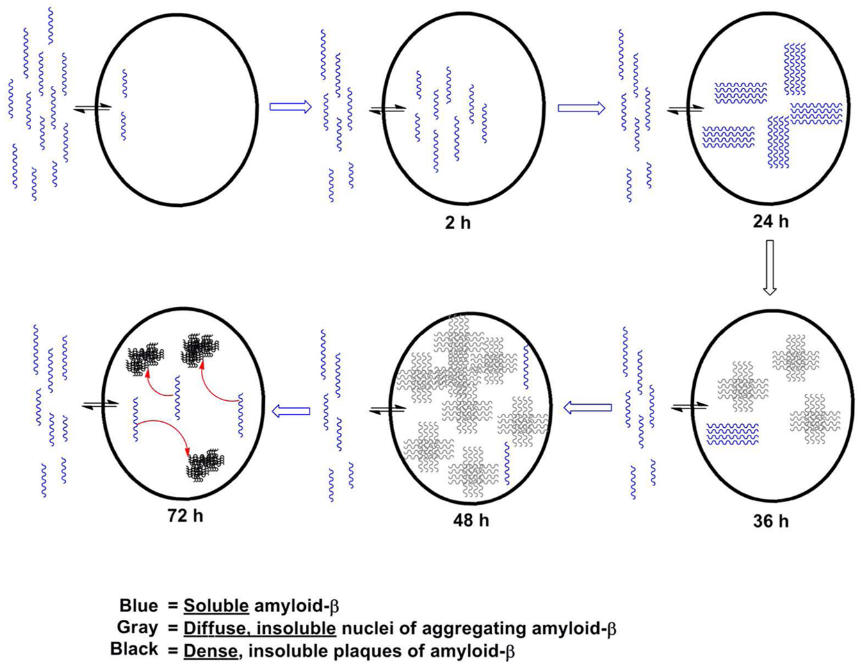

Figure 3. Proposed model for the observed light extinction variation in hyperspectral imaging spectra over time during amyloid invasion and intracellular aggregation. Diffuse low order aggregates or protofibrils of colloidal size increase until 48 h (resulting in increased scatter), beyond which fibril or plaque formation causes increased absorption or reflectance (leading to apparent light extinction in dark-field conditions).

with Aβ^{1-42} peptide itself. Upon Aβ^{1-42} treatment, HSI spectra of the cells over the 400−1000 nM region (Figure 1) exhibited extinction of wavelengths between 450 and 550 nm relative to cells treated with scr-Aβ^{1-42}. Sample standard deviations in these data over the entire wavelength range are depicted in Figure S1 (Supporting Information). The wavelength range of 480−530 nm carried deviations that satisfied the predefined criterion for significance ($p < 0.05$). This effect commenced at 4 h post-treatment and reached its peak at 48 h (Figure 2). Past the 48 h mark, extinction progressively decreased with that at 72 h tending toward the negative control. Volume of inoculum being held constant (1 mL), this extinction could be reproduced only at concentrations ≥ 250 nM (Supporting Information, Figure S2). This progressive extinction has two components: scattering and absorption. Scattering is a noncolligative property (i.e., a function of each distinct particle) influenced by particle size and polarizability (which implicates the physical and chemical constitution of the particle). Net absorption depends on the permittivity of the medium along the light propagation path, making it dependent on physical and chemical constitution of a particle. Figure 3 illustrates a possible model for the temporally varying extinction between 480 and 520 nm. From 0−24 h, $A\beta^{1-42}$ diffuses into the cell. Aggregation may very well occur during this period, but its optical effects are either nonexistent or are not detectable through our technique. Between 24 and 48 h, aggregation reaches orders that correspond to particle sizes and molecular conformations capable of scatter. Low order aggregates (≤ 55 nm) can lead to a high degree of Rayleigh scattering in the wavelength region subject to extinction in this experiment (scattering efficiency $\propto \lambda^{-4}$). While Rayleigh scattering would be even higher below 480 nm, the content of this wavelength in the source lamp (halogen−quartz aluminum reflector) is relatively negligible. The particle sizes of the aforementioned soluble $A\beta^{1-42}$ aggregates including the pathogenic globulomers, protofibrils, and globular colloids with polarizable α-sheets can lie in the Rayleigh size regime.[25] Particle size-dependent Mie scattering by larger particles in the 300−600 nm range (large protofibrils and insoluble fibrils) would also be relevant with greater scattering at wavelengths close to the particle size.[26] The latter type of scattering, if present, would be a relatively lesser contributor to extinction since its directionality is clustered in the direction of light propagation (forward scatter, but with deflection away from the path of the incident beam), while Rayleigh scattering occurs equally in all directions. At 48 h, the population density of $sA\beta^{1-42}$ oligomers causing the extinction is maximal. The decrease of extinction beyond this point may be a result of the following two events: (1) Coalescence begins, involving collapse of metastable protofibrils into fibrils and aggregation of fibrils into increasingly higher orders. The total quantity of available $A\beta^{1-42}$ being limited by the amount of inoculum, increased density of aggregates would mandate decrease in the exposed surface area of each aggregate that was responsible for extinction (and thus, extensive clearing of cytoplasm). (2) Mie scattering increasingly becomes the predominant contributor to extinction and therefore leads to a net reduction in extinction because of lowered backscatter and greater scatter in directions aligned with the forward direction.

The model proposed may be simplistic; cytoskeletal damage due to accumulating amyloid can also change optical properties and so can leakage of cytoplasmic content caused by amyloid induced cell membrane damage. An entry into attributions of such damage to specific spectral features is not readily apparent (at least to us). The time-dependent spectral change described above may prevail in all techniques utilizing HSI imaging for molecular aggregations. It would seem then that all HSI-based imaging should be interpreted in the light of the possibility of a false-negative based on the phenomenon apparent in this experiment. Cell structure damage in the intact animal from chronic $A\beta$ exposure has not been accounted for yet in this experiment; additional spectral artifacts and anomalies are to be expected.

Specificity of the HSI Spectral Signature. The change in light absorbance between the 400 and 1000 nM wavelength range in the HSI spectra of cells (specifically, between 480 and 550 nm) exposed to $A\beta^{1-42}$ appears to be highly specific for the aggregation-prone form of the peptide, because the sequence-scrambled form of $A\beta^{1-42}$, although accumulating (but not aggregating) to an equal extent inside the cell, fails to produce the characteristic HSI spectral shift. On the other hand, not enough information is apparent to us from these results to ascribe a specific spectral feature to a specific class of aggregate.

Utility of the HSI Spectral Signature in Inhibitor Screening. Having identified a unique HSI signature for $A\beta^{1-42}$, it was tempting to test the utility of this finding for screening of inhibitors. Guanidine, guanosine, and urea are known to obstruct amyloid aggregation through sequestration of electrophilic species that form amyloidogenic advanced glycation end-products (AGEs) with proteins.[27−29] Cells co-incubated with these inhibitors showed attenuation of amyloid-induced HSI spectral change, with some reaching that of cells not treated with $A\beta^{1-42}$ (Figure 4). The magnitude of signature-attenuation corresponded to the reported potency of the test inhibitor; thus, guanidine was found to afford the greatest attenuation in HSI spectral change followed sequentially by guanosine and urea.

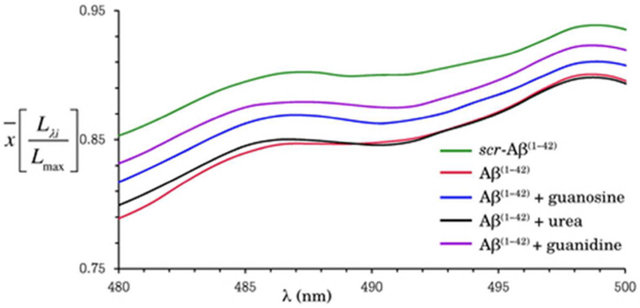

Figure 4. HSI spectra of the cytoplasm of SH-SY5Y cells incubated with $A\beta^{1-42}$ for 48 h in the presence of known $A\beta^{1-42}$ aggregation inhibitors (1 mM). The 480−500 nm portion that bore statistically significant normalized intensity differences is magnified to showcase spectral changes. Magnitude of scattered light deviation in $A\beta^{1-42}$-treated cells is inversely proportional to inhibitor potency.

HSI Spectral Signatures in Amyloid Aggregate Mapping and Quantitation. Spectral angle comparison, as described at length in Methods, allows for the comparison of two spectra by expressing them as vectors and calculating the angle between them from a simple dot product. The software front for the HSI instrumentation used in this study (ENVI, version 4.4) implements natively the calculation of spectral angles and comparison across matrices of spectral angles (the spectral angle mapper (SAM)). We accumulated a library of spectra cast by 50 distinct aggregates with a minimum of 10 pixels within an aggregate. The spectra were derived from incubation of SH-SY5Y cells with FITC-labeled $A\beta^{1-42}$ to directly visualize the local concentrations of the peptide, and at 48 h, HSI spectra of the detected $A\beta^{1-42}$ clusters were collected. The values of spectral map of various aggregates were qualitatively similar, attesting to the spectral features being defining characteristics of $A\beta^{1-42}$ aggregates. It follows that detection of such a spectral feature within an unknown specimen strongly suggests the presence of $A\beta^{1-42}$. As a test case, we exposed cells to a known amyloid aggregation inhibitor (guanidine) and a known amyloid aggregation promoter (Zn^{2+}).[30] The number of intracellular amyloid aggregates was

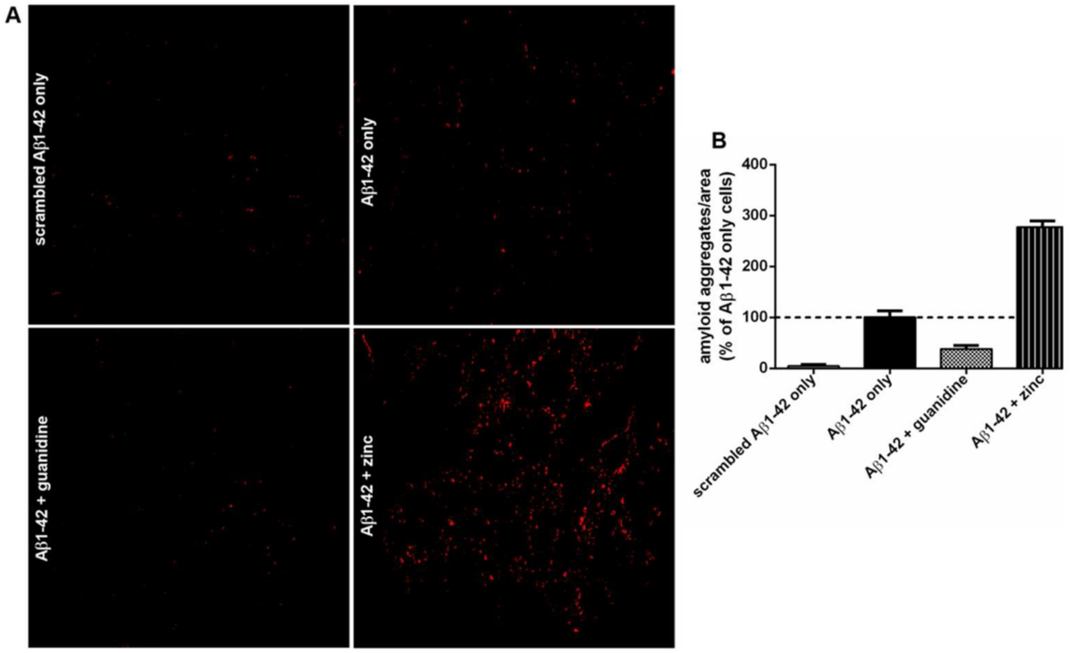

Figure 5. (A) Effects of $A\beta^{1-42}$ aggregation inhibitors and promoters on the levels of higher order $A\beta^{1-42}$ oligomers in SH-SY5Y cells. The cells were treated with FITC−$A\beta^{1-42}$ for 48 h in the presence of an aggregation promoter (zinc, 100 μM) and inhibitor (guanidine, 1 mM), and hyperspectral scans were acquired at the end of the experiment. The presence and location of Aβ1−42 aggregates was identified correctly by spectral angle mapping (SAM), whereby a spectral library of FITC−$A\beta^{1-42}$ aggregate was compared with the treated cells and the matching pixels are colored red. (B) Numerical representation of results from panel A. The number of red dots per unique area of an HSI image for each treatment group were plotted as a percentage of $A\beta^{1-42}$ exposed cells that were not treated with inhibitors.

lowered to 62% in the case of cells treated with guanidine (Figure 5) compared with cells treated with $A\beta^{1-42}$ alone. This number rises to 280% in case of Zn^{2+} treated cells, demonstrating that HSI coupled with spectral signature matching is able to differentiate between amyloid aggregation promoters and inhibitors. The implied ability to characterize compounds for their propensity to perturb or promote amyloidogensis is being used currently in our drug discovery program.

Ex Vivo Amyloidogenesis Observation Employing HSI. HSI spectral signatures from brain samples of patients with AD (full blown) varied from those acquired from age-matched normal individuals (Figure 6A). The pattern of spectral variation with respect to wavelength was similar to the characteristic differences observed between normal cells and $A\beta^{1-42}$ treated cells. Total scattering in the samples from Alzheimer's patients was lower, reflecting dispersion of amyloid aggregates and accompanying morphological and biochemical changes. Examination of retinal tissue samples from normal and Alzheimer's afflicted patients offered similar results (Figure 6B).

Diagnostically, the retina can be considered an extension of the CNS that offers noninvasive access. Consequently, retinal imaging is an emerging mode of identification of neurodegenerative disorders like AD.[31] The consistent, reproducible, and tangible differences observed in retinal samples in the present experiments and, importantly, the lack of a requirement for an extraneous xenobiotic encouraged us to explore their utility for diagnosis of AD and eAD. Progress toward this goal began with the *ex vivo* imaging of retinae from transgenic APP/PS1 mice with the HSI technique as described in Methods. HSI spectra of mouse brain tissue and retinae were acquired at 2, 4, 6, and 8 months of age (Figure 7). Differences between normal and APP/PS1 mice retinae reached the predefined statistical significance criterion ($p < 0.05$) at 4 months of age, and continued to increase with age. At 4 months of age, amyloid aggregates were not detected in the brains of the transgenic Alzheimer's or normal mice (Figure 8B). At 6 months and onward, the spectral differences between the WT and transgenic APP/PS1 mice grew exponentially (Figure 8C). At

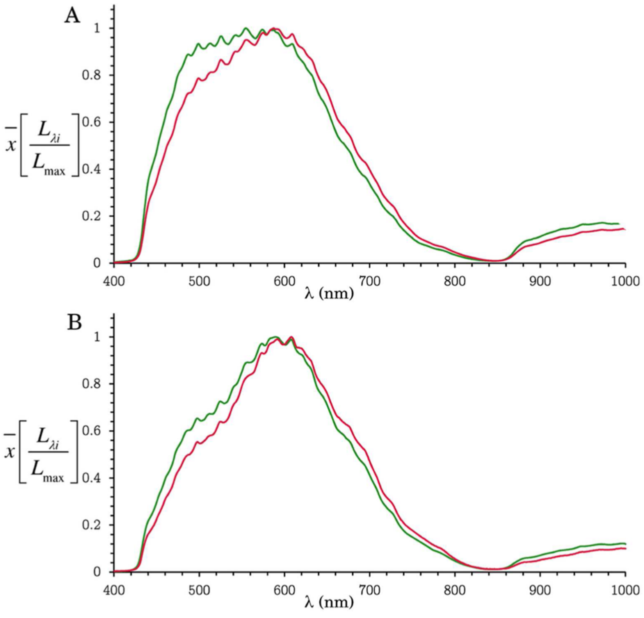

Figure 6. (A) Differences between the HSI spectra of Alzheimer's-afflicted and normal human brain tissue. (B) Differences between the HSI spectra of Alzheimer's-afflicted and normal human retina. Variations are most prominent for wavelengths between 450 and 580 nm (green, normal tissue; red, Alzheimer's tissue).

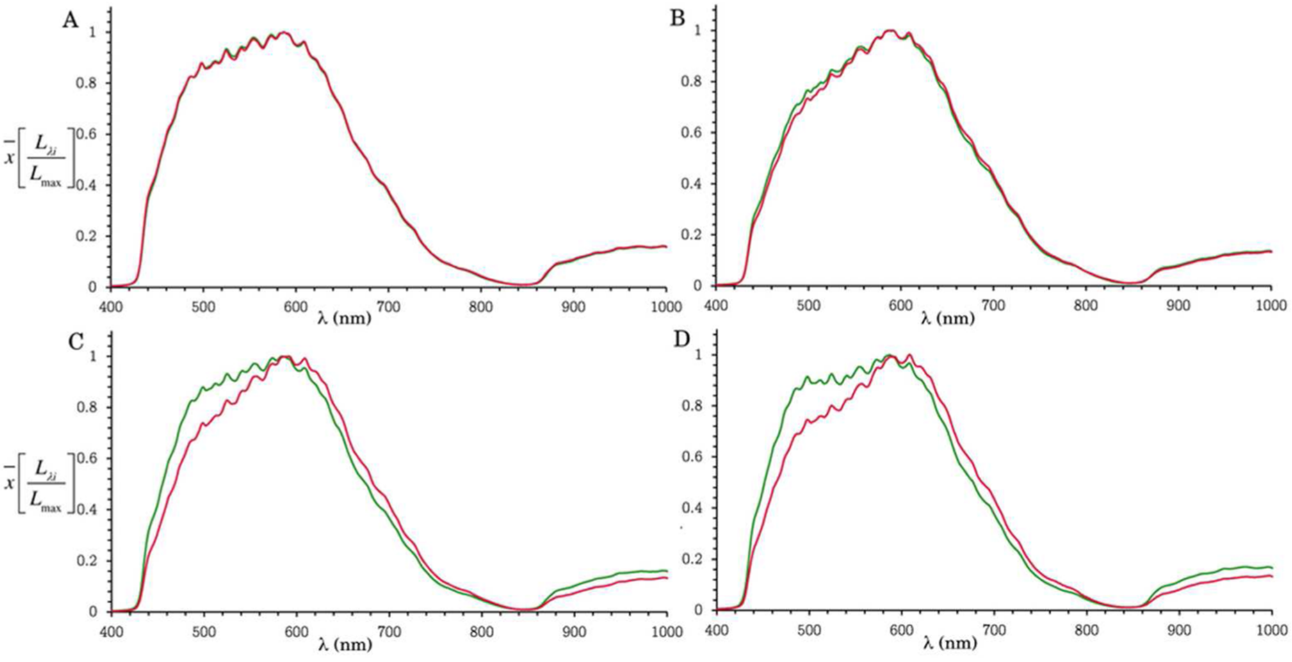

Figure 7. HSI spectra of retinae isolated from wild type (green) and APP/PS1 (red) mouse at (A) 2, (B) 4, (C) 6, and (D) 8 months of age ($n = 6$). Consistent and progressive variation is seen for scattering of wavelengths between 480 and 560 nm.

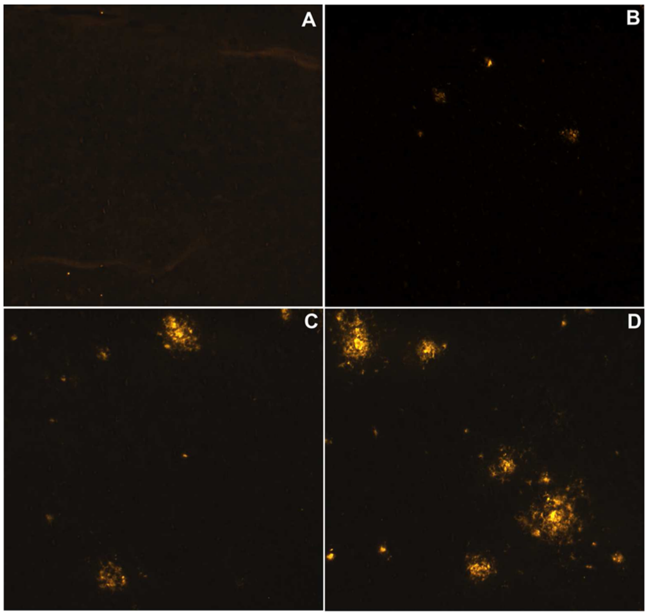

Figure 8. Fluorescent Aβ^{1-42} antibody-stained brain tissue from WT (A) and APP/PS1 mouse (B = 6 months, C = 7 months, D = 8 months). While staining of APP/PS1 mouse brain is hardly noteworthy at six months, that at eight months shows alarmingly increased number and size of Aβ plaques. The details of the antibody used and the protocol for immunohistochemistry are described under Methods.

8 months, spectral differences became glaringly obvious, at which time plaque was clearly observable in brain tissue (Figure 8D). Thus-demonstrated is the independence of HSI spectral differences in the retina from frank amyloid plaque deposition in the brain. Early detection of amyloidogenesis independent of symptomology is paramount to the development of a successful (i.e., curative) address for Alzheimer's disease, since even early Alzheimer's disease reflects metastasized amyloid aggregates and portends irreversible destruction of neuronal tissue. To this end, the detection of amyloid HSI signature in the retina warrants aggressive developmental pursuit.

Retinal vasculature dystrophy,[32] retinal cell loss and denervation, and overt Aβ^{1-42} deposits in retinal tissue of transgenic APP/PS1 mice[33−35] have been reported in the past as representative of early onset Alzheimer's disease. Koronyo-Hamaoui et al.'s elegant demonstration[31] of curcumin-staining of retinal Aβ followed by imaging shows that retinal plaques are present (and were detected) as early as 2.5 months of age, while brain Aβ aggregates were detectable only after 5−6 months in APP/PS1 APP/PS1 mice. Our findings, although derived from a technique based on a completely different physical principle, corroborate that retinal Aβ can be observed far before overt plaque deposition in the brain of the APP/PS1 transgenic mouse. A reviewer made us aware of the possibility of using tomographical data for amyloid characterization in the retina. Optical coherence tomography (OCT) is a well-known tool for the measurement of reticular nerve fiber layer (RFNL) thickness and topography. To our understanding, the current axial resolution achieved during clinical ophthalmic OCT imaging has reached the single-digit micrometer range.[36] Spectral domain OCT could potentially be an excellent complementary technique to HSI signature-mapping since the former would yield physical parameters of the optical feature being characterized.

An ongoing treatment program with our experimental anti-Alzheimer's drug candidate, ψ-GSH, presented us the opportunity to monitor differential Alzheimer's progression in real time.[37] Wild-type (WT) mice (10, female) and transgenic (APP/PS1) mice (two groups, 10 females treated with ψ-GSH and another 10 females treated with vehicle control) were employed. ψ-GSH was administered for 12 weeks (ip) to the treatment group beginning at three months of age. Every 4 weeks, retinae of two mice from all three groups were isolated and HSI spectra were acquired according to the technique described in Methods (Figure 9). One month following

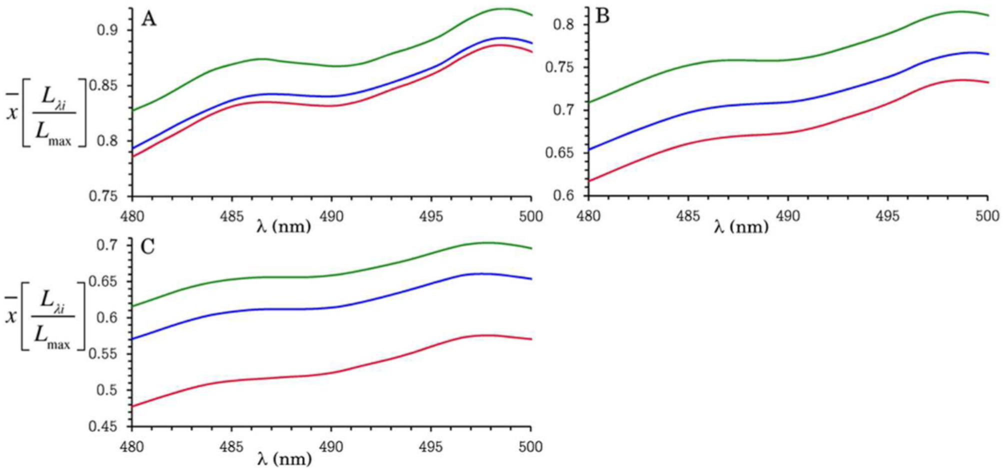

Figure 9. Monitoring of drug treatment effects in APP/PS1 mice retinae by HSI. An advanced candidate therapeutic, ψ-GSH, was administered to age-matched APP/PS1 and WT mice ip for 12 weeks. Panels A, B, and C demonstrate a mean of spectral images acquired after 1, 2, and 3 months of drug treatment, respectively, and compared with vehicle controls in APP/PS1 and WT groups. Green, saline treated WT mice; red, saline treated Alzheimer's mice; blue, Alzheimer's mice + ψ-GSH ip. Shift in the HSI spectral pattern of the retinae of drug-treated mice from closer to the pattern from the APP/PS1 group, progressively toward that from the WT group suggested positive outcome of the treatment. This was corroborated by the results of cognition test and $A\beta^{1-42}$ immunohistochemistry on the brain tissue.[37]

treatment initiation, retinae from the two transgenic mouse groups did not exhibit statistically significant differences. However, the differences between the transgenic mouse retinae and the age-matched WT mouse retinae were significant. HSI spectra from the retina of the ψ-GSH treated mice began to differ from the APP/PS1 mice at 2 months of treatment. The spectra from the retinae of mice treated with ψ-GSH tended toward those from normal mice. This difference persisted throughout the experiment until the end of the treatment.

At the conclusion of the preclinical study, we examined the relationship between retinal HSI spectra and cognitive-histochemical parameters (reported elsewhere[37] but summarized briefly here). Cognitive aspects were quantified using the Morris water maze, which regards the escape latency and path length for successful memory recall of a stationary object as cognitive parameters.[38] Wild-type (WT) mice and ψ-GSH ip treated mice were subject to successful learned behavior inculcation, as exemplified by escape latencies significantly lower than and path lengths significantly shorter than saline treated transgenic mice. HSI scans of the WT and ψ-GSH treated mice did not show retinal HSI signatures indicative of amyloidopathy, while the saline control transgenic mice did. Across the same groups, Aβ load was quantitated by staining brain sections with anti-Aβ antibody. Untreated mice whose brain showed significant amyloid load also afforded amyloidogenesis-positive HSI signatures, which were in turn negative for ψ-GSH treated transgenic mice with insignificant amyloid load.

Conclusion and Future Directions. As it stands, we believe that HSI spectral imaging is sufficiently validated as a modality for (1) *ex vivo* Aβ aggregate detection in mouse brain and retina, (2) *ex vivo* monitoring of treatment progress in mouse retina, and (3) *in vitro* screening of chemical entities for amyloidogenesis modulatory activity. Of particular note is the independence from an externally applied or administered labeling agent. The detection of amyloid aggregates in the retina well before brain plaque deposition attests to the technique's sensitivity. Acquisition of a unique signature for Aβ plaque attests to its specificity. These findings have served as the basis for an extensive ongoing program on *in vivo* HSI imaging of live mouse retina. Preliminary experiments employing a spectral imaging instrument devised to look directly into live mouse eye revealed (after a large number of instrumental and algorithmic modifications) spectral trends in live transgenic mouse similar to those found in isolated retinas. This very encouraging follow-up will be presented in a subsequent report.

■ METHODS

Reagents. $A\beta^{1-42}$, scrambled $A\beta^{1-42}$, FITC–$A\beta^{1-42}$, and FITC–scrambled-$A\beta^{1-42}$ were purchased from American Peptide Company (Sunnyvale, CA, USA). All other chemicals were purchased from Sigma (St. Louis, MO, USA). For all experiments, a stock solution of $A\beta^{1-42}$ (1 mg/mL) prepared in 1,1,1,3,3,3-hexafluoro-2-propanol (HFIP) was sonicated in a water bath at ambient temperature for 10 min and dried under vacuum. The HFIP-treated $A\beta^{1-42}$ was then dissolved in dimethyl sulfoxide (DMSO) to a final concentration of 1 mM before storage at −20 °C. Stock solutions of scrambled $A\beta^{1-42}$, FITC–$A\beta^{1-42}$, and FITC–scrambled-$A\beta^{1-42}$ were prepared in a similar manner. The cell culture media minimum essential medium (MEM), F12, and fetal bovine serum (FBS) were obtained from Invitrogen (Carlsbad, CA).

Cell Culture and Cellular Uptake. All the cell culture experiments described in the present study employed a human neuroblastoma cell line, SH-SY5Y, which was obtained from American Type Culture Collection (Manassas, VA). The cells were maintained in MEM/F12 (1:1) medium supplemented with 10% FBS, 100 units/mL penicillin, 100 units/mL streptomycin, and 1% NEAA (nonessential amino acids). Cells were grown at 37 °C in a humidified atmosphere with 5% CO_2. $A\beta^{1-42}$ and scrambled-$A\beta^{1-42}$ were added to SH-SY5Y cultures for 24 h. For time-dependence experiments, 250 nM $A\beta^{1-42}$ was added to SH-SY5Y cells plated in 4-well Lab-Tek chamber slides (Nunc), and images as well as HSI spectral scans were acquired at varying times (0−7 days) after addition of the labeled-$A\beta^{1-42}$. For dose-dependence experiments, $A\beta^{1-42}$ and FITC–$A\beta^{1-42}$ were added at varying concentrations (0−1000 nM), and cells were imaged 24 h thereafter. In some experiments, SH-SY5Y cells were incubated with FITC–$A\beta^{1-42}$ for 48 h in the presence and absence of inhibitors or promoters of β-amyloid peptide.

Hyperspectral Imaging Principles and Instrumentation.[39] *Illumination Technique.* This technique is illustrated in Figure 10. The image of the source is eliminated by passing the light through a liquid light-guide (eliminating source image). Emergent rays are allowed to expand to the desired diameter and collimated. A diffuser

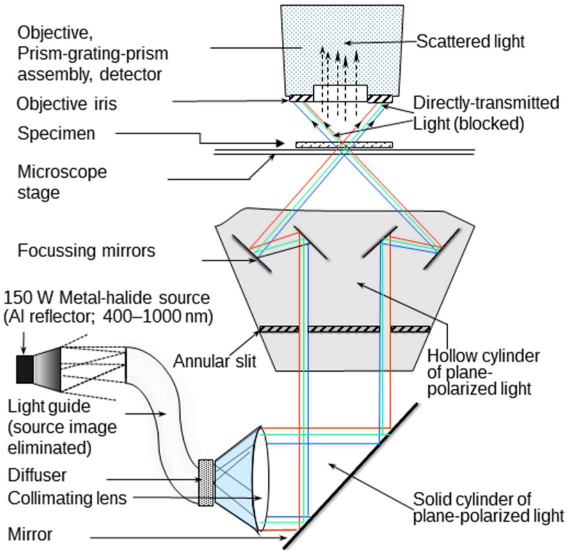

Figure 10. Schematic light-path diagram of the instrument used for hyperspectral imaging. For clarity, the condenser components beneath the specimen/microscope stage have been represented by two pairs of mirrors (these would be a series of lenses).

then produces a solid cylinder of collimated, diffuse light that is reflected by 90° onto an annular slit that blocks all but the periphery of the light cylinder. A hollow cylinder of light thus proceeds to the condenser assembly that converges it into a hollow cone. The specimen is placed at the focal point of this cone, effectively achieving convergence of all light into one intense spot. Adjustment of a focused objective lens above the specimen to a numerical aperture (NA) of ≤ 1.2 with a diaphragm restricts passage of light to only that emerging from scatter (i.e., "dark-field" conditions are implemented).

Spectrophotometry. A holographic grating (sandwiched between two prisms) receives, diffracts, and projects light onto a detector array. The direction of the resultant light propagation being a function of incident wavelength, the spatial location of the light incident on the detector array is used to generate a set of monochromatic points of varying intensity corresponding to locations on the specimen. This arrangement provides for a spectral resolution of 2.5 nm through a 30 μm slit. The actual image pixel size attained with a 40× objective (2 × 2 binning) is 322 nm × 322 nm.

$$\text{pixel dimensions} = \frac{\text{objective magnification} \times \text{binning}}{\text{camera pixel size} \times \text{lens magnification} \times \text{c-mount}}$$

The spectrum of light scattered during transmission through the specimen, which contains effects of light absorption, is obtained at each image pixel. In the present study, the 400−1000 nm wavelength region was scanned, yielding intensity readings at 467 well-resolved wavelengths.

At any given point of time, a single line along the x axis of the specimen (first spatial dimension) is subjected to spectral quantification (spectral "dimension"). Movement of the sample stage along the y axis (at 90° to the irradiated line) yields the second spatial dimension, yielding three-dimensional spatiospectral stack.

Data Acquisition and Processing. Environment for Visualization (ENVI), version 4.4 (Exelis, McLean, VA), served as the software front for directing spectral acquisition. Five regions of interest (ROIs) consisting of randomly selected groups of ≥ 150 pixels each were scanned with the aforementioned optical arrangement. In order to render data suitable for comparison across different samples, intensities at each wavelength were subjected to two corrections: (1) for "dark current" aberrations, through subtracting values obtained without illumination, and (2) for differing mass extinction coefficients across ROIs, by expressing intensity emitted by the illuminated sample at each wavelength as a fraction of the intensity at the most intense wavelength in that ROI. In other words, the parameter whose variation with wavelength is being studied here is $L_{\lambda_i}/L_{\lambda_{\max}}$, where L_{λ_i} and $L_{\lambda_{\max}}$ correspond to the emergent intensity at the ith wavelength and at the wavelength that is maximally intense. Distance of the sample from the objective and intensity of incident light being held constant, this parameter is inversely proportional to the ratio of the exponents of the mass extinction coefficients at the respective wavelengths ($L_{\lambda_i}/L_{\lambda_{\max}} \propto \mathrm{e}^{-\mu_\lambda}/\mathrm{e}^{-\mu_{\max}}$). Standard errors in the mean values at each wavelength from the five ROIs/specimen (triplicate readings) yielded p-values less than 0.05. Scatter plots ($\overline{x}(I_\lambda/I_{\max})$ vs λ) of the specimen and the corresponding control (data from specimens exposed to scr-Aβ^{1-42}) were overlaid. The refined data were utilized for comparison with a spectral library of FITC−Aβ^{1-42} aggregate. The latter was prepared by recording the spectra of intracellular Aβ^{1-42} aggregates.

The spectral "signature" of an optical feature in a specimen is the pattern of intensity variance across distinct wavelengths within the same spectrum. A true pattern is necessarily invariant with multiplicative intensity scaling (i.e., the relative intensity ratios between wavelengths of a particular pattern should remain constant irrespective of absolute magnitudes). Such scaling can emerge from specimen illumination intensity, nonuniformity of illumination, varying optical density arising from dissimilar specimen thickness, and fluctuations in detector sensitivities that are uniform across the entire wavelength range. We employed the "spectral angle (SA)" metric for coalescing the spectra into a single scalar quantity. It can be described in the current context as follows: (1) a spectrum emerging from a single pixel is considered to be a vector with dimensions equal to the number of wavelengths and the components in each dimension equal to the respective intensities, (2) the inner product of the two vectors is stated, and the cosine of the angle between the two vectors (i.e., the cosine similarity) is calculated (eq 1). Since both wavelength and intensity are positive numbers, cos θ assumes values between 0 and 1. While a number of comparison indices exist that may be applicable to the present work, the spectral angle is one of the two most reliable indices (the other being the correlation coefficient) prefixed with "spectral".[40] Since (1) wavelength shifts (e.g., the detector erroneously reading light of wavelength a as that of wavelength b) are negated by repeated calibration and (2) a very small value of SA was assigned as the threshold for similarity, the SA was deemed most appropriate and sufficient.[41] By its definition, the spectral angle is inversely proportional to spectral pattern similarity. The spectral angle mapping (SAM) algorithm as implemented in ENVI was utilized to rapidly calculate the spectral angle between the spectrum of each pixel in a specimen and that of each pixel in a reference sample. A very narrow spectral angle threshold (0.1°) was regarded as a pixel "match".

$$\theta = \frac{180}{\pi} \arccos\left[\frac{\vec{s} \times \vec{r}}{\| \vec{s} \| \times \| \vec{r} \|}\right] = \frac{\sum_{\lambda=1}^{n} (L_{s\lambda} L_{r\lambda})}{\sqrt{\sum_{\lambda=1}^{n} (L_{s\lambda})^2} \times \sqrt{\sum_{\lambda=1}^{n} (L_{r\lambda})^2}} \qquad (1)$$

where $L_{s\lambda}$ and $L_{r\lambda}$ are luminosities of the sample (s) and the reference (r) at the wavelength λ.

Animals. Female APP and PS1 double transgenic mice (6−8 weeks old, catalogue no. 005864) and WT C57BL6 mice were purchased 2 weeks before use from Jackson Laboratories (Bar Harbor, ME) and housed in SPF conditions, which included filtered air and sterilized food, water, bedding, and cages. All experiments were approved by the Institutional Animal Care and Use Committee at the University of Minnesota. All experimental and animal handling procedures were in accordance with national ethical guidelines. Mice were maintained on standard food and water *ad libitum.*

Hyperspectral Analysis of Mouse Brain and Retina. Brain and retina tissues were isolated from transgenic Alzheimer's and age-matched WT mice at 2, 4, 6, and 8 months of age (six mice).

Isolation and Analysis of Brain Tissue. Brains were removed from WT and APP/PS1 mice and postfixed in Zamboni's fixative (4%

paraformaldehyde (PFA) and 15% picric acid in 0.25 M sodium phosphate, pH 7.5) for 48 h before being cryopreserved in a 30% (wt/vol) sucrose/0.1 M sodium phosphate-buffered saline (PBS) solution. Frozen sections (10 μm) in OCT were cut on a sliding microtome and brought to room temperature, and covered with hardset Vectashield mounting medium with the nuclear stain DAPI (catalogue no. H-1500; Vector Laboratories, Burlingame, CA). The whole-mount brain slides were scanned with a Cytoviva microscope, and spectral signatures were collected from wavelengths in the 400−1000 nm range as described before.

Isolation and Analysis of Retina Tissue.[42] Eyes were enucleated from WT and APP/PS1 mice at the desired age. For whole-mount retinas, eyes were fixed in ∼2 mL of freshly prepared 4% PFA−PBS at room temperature for 45 min. This was followed by washing with ice-cold PBS solution (2 mL) at least five times. The anterior eye portion, cornea, was dissected out under a surgical microscope. The iris was then removed followed by the sclera, lens, and hyaloid vessels. The isolated retinas were then washed with ice-cold PBS and divided into four quadrants by making four radial incisions. The whole mounts were prepared by transferring the dissected retinas onto a microscope slide and covering with hardset Vectashield mounting medium with the nuclear stain DAPI. The whole-mount retina slides were scanned with the Cytoviva microscope, and spectral signatures were collected from wavelengths in the 400−1000 nm range as described before.

Immunohistochemistry of Mouse Brain and Retina Samples.[37] For immunofluorescence studies, brain section slides and retina sample slides were preincubated for 1 h in 5% normal goat serum (NGS) in 1× PBST (1× PBS containing 0.3% Triton X-100) at room temperature. A primary antibody against β-amyloid peptide (Cell Signaling, Cat. no. 2454) was employed at a dilution of 1:200 in 1% NGS in 1× PBST. After an overnight incubation at 4 °C, the slides were rinsed 3 times for 10 min with 1× PBST and then incubated for 2 h in goat anti-rabbit IgG conjugated to Cy3 diluted to 1:1000 in 1% NGS in 1× PBST. The sections were rinsed in PBST 3 times for 10 min and in PBS for 5 min. Samples were then dehydrated in ethanol, cleared with methyl salicylate, and mounted in DEPEX (Electron Microscopy Science, Poole, UK), and the staining of β-amyloid aggregates and plaques was visualized with the Cytoviva microscope.

Hyperspectral Imaging To Follow Drug-Treatment Outcomes in APP/PS1 Mice. As reported previously,[37] we treated APP/PS1 and WT mice with our lead candidate drug, ψ-GSH, 3×/week for 12 weeks beginning at 3−4 months of age. The study was divided into three 10-mice groups: group 1, APP/PS1 mouse (vehicle control); group 2, APP/PS1 mouse (ψ-GSH ip 500 mg/kg); group 3, WT mouse (vehicle control). At the end of the study, animals were euthanized, and retinae were isolated from animals in each group followed by hyperspectral imaging as described under Hyperspectral Analysis of Mouse Brain and Retina.

Statistical Analysis of Data. Spectral data were analyzed to characterize differences between cells treated with β-amyloid peptide and untreated cells in the presence or absence of inhibitors. The differences between the normalized mean intensities at each wavelength for samples under various treatments were compared by the unpaired Student's t test (two-tailed test) or the multivariate analysis of variance (ANOVA), as appropriate. Values for each wavelength were reported as means ± SD. A p value lower than 0.05 was considered as indicative of significant difference. Similarly, for tissue samples, spectral differences between Alzheimer's and WT mouse tissue at a particular time point were analyzed by the unpaired Student's t test with $p < 0.05$ considered to indicate differences of significance.

■ ASSOCIATED CONTENT

Ⓢ Supporting Information

Plot of corrected sample standard deviations vs wavelengths, a portion of a HSI spectrum corresponding to Figure 1 showing error bars at each wavelength, and plot showing dependence of the HSI spectrum on the exposure concentration of $A\beta^{1-42}$. This material is available free of charge via the Internet at http://pubs.acs.org.

■ AUTHOR INFORMATION

Corresponding Author

*Robert Vince. Mailing address: Center for Drug Design, MMC 204 Mayo, 8204A (Campus Delivery Code), 420 Delaware St SE, Minneapolis, MN 55455. Tel. 612-624-9911. Fax: 612-626-2633. E-mail: vince001@umn.edu.

Author Contributions

All authors have contributed equally to this manuscript.

Funding

This research was supported by the funds from the Center for Drug Design at the University of Minnesota.

Notes

The authors declare the following competing financial interest(s): A patent application on hyperspectral imaging for early detection of Alzheimer's disease has been filed by the University of Minnesota with R.V. and S.S.M. named inventors.

■ ACKNOWLEDGMENTS

We thank Dr. James Beach, Technical Development Director, Cytoviva Inc., for helping us understand the engineering fundamentals of the imaging equipment used in this work. We also thank Prof. Marna Ericson of the Department of Dermatology at the University of Minnesota for technical assistance while working with the Cytoviva Hyperspectral Imaging System.

■ REFERENCES

(1) Herczenik, E., and Gebbink, M. F. (2008) Molecular and cellular aspects of protein misfolding and disease. *FASEB J. 22*, 2115−2133.

(2) Yerbury, J. J., Stewart, E. M., Wyatt, A. R., and Wilson, M. R. (2005) Quality control of protein folding in extracellular space. *EMBO Rep. 6*, 1131−1136.

(3) Moore, R. A., Taubner, L. M., and Priola, S. A. (2009) Prion protein misfolding and disease. *Curr. Opin. Struct. Biol. 19*, 14−22.

(4) Bruce, A., Bray, D., Hopkin, K., Johnson, A., Lewis, J., Raff, M., Roberts, K., and Walter, P. (2010) Protein Structure and Function, in *Essential Cell Biology*, 3rd ed., pp 120−170, Garland Science, Taylor and Francis Group, New York.

(5) Selkoe, D. J. (2003) Folding proteins in fatal ways. *Nature 426*, 900−904.

(6) Costanzo, M., and Zurzolo, C. (2013) The cell biology of prion-like spread of protein aggregates: Mechanisms and implication in neurodegeneration. *Biochem. J. 452*, 1−17.

(7) Selkoe, D. J. (2004) Cell biology of protein misfolding: The examples of Alzheimer's and Parkinson's diseases. *Nat. Cell Biol. 6*, 1054−1061.

(8) Lesne, S. E., Sherman, M. A., Grant, M., Kuskowski, M., Schneider, J. A., Bennett, D. A., and Ashe, K. H. (2013) Brain amyloid-beta oligomers in ageing and Alzheimer's disease. *Brain 136*, 1383−1398.

(9) Modler, A. J., Gast, K., Lutsch, G., and Damaschun, G. (2003) Assembly of amyloid protofibrils via critical oligomers—a novel pathway of amyloid formation. *J. Mol. Biol. 325*, 135−148.

(10) Walsh, D. M., Lomakin, A., Benedek, G. B., Condron, M. M., and Teplow, D. B. (1997) Amyloid beta-protein fibrillogenesis. Detection of a protofibrillar intermediate. *J. Biol. Chem. 272*, 22364−22372.

(11) Yoshimura, Y., Lin, Y., Yagi, H., Lee, Y. H., Kitayama, H., Sakurai, K., So, M., Ogi, H., Naiki, H., and Goto, Y. (2012) Distinguishing crystal-like amyloid fibrils and glass-like amorphous aggregates from their kinetics of formation. *Proc. Natl. Acad. Sci. U.S.A. 109*, 14446−14451.

(12) Roychaudhuri, R., Yang, M., Hoshi, M. M., and Teplow, D. B. (2009) Amyloid beta-protein assembly and Alzheimer's disease. *J. Biol. Chem. 284*, 4749−4753.

(13) Kagan, B. L., Hirakura, Y., Azimov, R., Azimova, R., and Lin, M. C. (2002) The channel hypothesis of Alzheimer's disease: current status. *Peptides 23*, 1311−1315.

(14) Miller, Y., Ma, B., Tsai, C. J., and Nussinov, R. (2010) Hollow core of Alzheimer's Aβ42 amyloid observed by cryoEM is relevant at physiological pH. *Proc. Natl. Acad. Sci. U. S. A. 107*, 14128−14133.

(15) Li, J. J., Dolios, G., Wang, R., and Liao, F. F. (2014) Soluble beta-amyloid peptides, but not insoluble fibrils, have specific effect on neuronal microRNA expression. *PLoS One 9*, No. e90770.

(16) Tomiyama, T. (2010) Involvement of beta-amyloid in the etiology of Alzheimer's disease. *Brain Nerve 62*, 691−699.

(17) Vellas, B., Carrillo, M. C., Sampaio, C., Brashear, H. R., Siemers, E., Hampel, H., Schneider, L. S., Weiner, M., Doody, R., Khachaturian, Z., Cedarbaum, J., Grundman, M., Broich, K., Giacobini, E., Dubois, B., Sperling, R., Wilcock, G. K., Fox, N., Scheltens, P., Touchon, J., Hendrix, S., Andrieu, S., Aisen, P., et al. (2013) Designing drug trials for Alzheimer's disease: What we have learned from the release of the phase III antibody trials: a report from the EU/US/CTAD Task Force. *Alzheimer's Dementia 9*, 438−444.

(18) Verdooner, S. (2013) Apparatus and method for imaging an eye, International Patent WO201111602A2.

(19) Groenning, M. (2010) Binding mode of Thioflavin T and other molecular probes in the context of amyloid fibrils-current status. *J. Chem. Biol. 3*, 1−18.

(20) Zovo, K., Helk, E., Karafin, A., Tougu, V., and Palumaa, P. (2010) Label-free high-throughput screening assay for inhibitors of Alzheimer's amyloid-beta peptide aggregation based on MALDI MS. *Anal. Chem. 82*, 8558−8565.

(21) McKoy, A. F., Chen, J., Schupbach, T., and Hecht, M. H. (2012) A novel inhibitor of amyloid β (Aβ) peptide aggregation: from high throughput screening to efficacy in an animal model of Alzheimer's disease. *J. Biol. Chem. 287*, 38992−39000.

(22) Ahn, B. W., Song, D. U., Jung, Y. D., Chay, K. O., Chung, M. A., Yang, S. Y., and Shin, B. A. (2000) Detection of β-amyloid peptide aggregation using DNA electrophoresis. *Anal. Biochem. 284*, 401−405.

(23) Hu, X., Crick, S. L., Bu, G., Frieden, C., Pappu, R. V., and Lee, J. M. (2009) Amyloid seeds formed by cellular uptake, concentration, and aggregation of the amyloid-beta peptide. *Proc. Natl. Acad. Sci. U. S. A. 106*, 20324−20329.

(24) Li, J., Kanekiyo, T., Shinohara, M., Zhang, Y., LaDu, M. J., Xu, H., and Bu, G. (2012) Differential Regulation of Amyloid-β Endocytic Trafficking and Lysosomal Degradation by Apolipoprotein E Isoforms. *J. Biol. Chem. 287*, 44593−44601.

(25) Quinten, M., and Stier, J. (1995) Absorption of Scattered Light in Colloidal Systems of Aggregated Particles. *Colloid Polym. Sci. 273*, 233−241.

(26) Veloso, A. J., Yoshikawa, H., Cheng, X. R., Tamiya, E., and Kerman, K. (2011) Optical Trapping for the Characterization of Amyloid-Beta Aggregation Kinetics. *Analyst 136*, 4164−4167.

(27) Vitek, M. P., Bhattacharya, K., Glendening, J. M., Stopa, E., Vlassara, H., Bucala, R., Manogue, K., and Cerami, A. (1994) Advanced glycation end products contribute to amyloidosis in Alzheimer's disease. *Proc. Natl. Acad. Sci. U. S. A. 91*, 4766−4770.

(28) Tilton, R. G., Chang, K., Hasan, K. S., Smith, S. R., Petrash, J. M., Misko, T. P., Moore, W. M., Currie, M. G., Corbett, J. A., McDaniel, M. L., and Williamson, J. R. (1993) Prevention of diabetic vascular dysfunction by guanidines. Inhibition of nitric oxide synthase versus advanced glycation end-product formation. *Diabetes 42*, 221−232.

(29) Subratty, A. H., Aukburally, N., Jowaheer, V., and Joonus, N. (2010) Vitamin C and urea inhibit the formation of advanced glycation end products in vitro. *Nutr. Food Sci. 40*, 456−465.

(30) Esler, W. P., Stimson, E. R., Jennings, J. M., Ghilardi, J. R., Mantyh, P. W., and Maggio, J. E. (1996) Zinc-induced aggregation of human and rat beta-amyloid peptides in vitro. *J. Neurochem. 66*, 723−732.

(31) Koronyo-Hamaoui, M., Koronyo, Y., Ljubimov, A. V., Miller, C. A., Ko, M. K., Black, K. L., Schwartz, M., and Farkas, D. L. (2011) Identification of amyloid plaques in retinas from Alzheimer's patients and noninvasive in vivo optical imaging of retinal plaques in a mouse model. *Neuroimage 54*, S204−S217.

(32) Berisha, F., Feke, J. T., Trempe, C. L., McMeel, J. W., and Schepens, C. L. (2007) Retinal abnormalities in early Alzheimer's disease. *Invest. Ophthalmol. Vis. Sci. 48*, 2285−2289.

(33) Blanks, J. C., Schmidt, S. Y., Torigoe, Y., Porrello, K. V., Hinton, D. R., and Blanks, R. H. (1996) Retinal pathology in Alzheimer's disease. II. Regional neuron loss and glial changes in GCL. *Neurobiol. Aging 17*, 385−395.

(34) Paquet, C., Boissonnot, M., Roger, F., Dighiero, P., Gil, R., and Hugon, J. (2007) Abnormal retinal thickness in patients with mild cognitive impairment and Alzheimer's disease. *Neurosci. Lett. 420*, 97−99.

(35) Parisi, V., Restuccia, R., Fattapposta, F., Mina, C., Bucci, M. G., and Pierelli, F. (2001) Morphological and functional retinal impairment in Alzheimer's disease patients. *Clin. Neurophysiol. 112*, 1860−1867.

(36) Drexler, W., Morgner, U., Ghanta, R. K., Kartner, F. X., Schuman, J. S., and Fujimoto, J. G. (2001) Ultrahigh-resolution ophthalmic optical coherence tomography. *Nat. Med. 7*, 502−507.

(37) More, S. S., Vartak, A. P., and Vince, R. (2013) Restoration of glyoxalase enzyme activity precludes cognitive dysfunction in a mouse model of Alzheimer's disease. *ACS Chem. Neurosci. 4*, 330−338.

(38) Morris, R. (1984) Developments of a water-maze procedure for studying spatial learning in the rat. *J. Neurosci. Methods 11*, 47−60.

(39) Aikio, M. (2001) Hyperspectral prism-grating-prism imaging spectrograph, Ph.D. Thesis, University of Oulu, Publ. 435, VTT Publications, Espoo, Finland.

(40) Robila, S. A. (2004) An analysis of spectral metrics for hyperspectral image processing. *Geoscience and Remote Sensing Symposium, IGARSS '04. Proceedings. 2004*, Vol. 5, pp 3233—3236, IEEE International, Piscataway, NJ.

(41) Zhang, J., Zhu, W., Wang, L., and Jiang, N. (2012) Evaluation of similarity measure methods for hyperspectral remote sensing data. *Geoscience and Remote Sensing Symposium (IGARSS), 2012*, pp 4138—4141, IEEE International, Piscataway, NJ.

(42) Pitulescu, M. E., Schmidt, I., Benedito, R., and Adams, R. H. (2010) Inducible gene targeting in the neonatal vasculature and analysis of retinal angiogenesis in mice. *Nat. Protoc. 5*, 1518−1534.